Numerical investigation on heat and mass transfer characteristics of inclined plate falling film absorption with nano-lithium bromide solution

Numerical investigation on heat and mass transfer characteristics of inclined plate falling film absorption with nano-Lithium Bromide solution

Gang Wang [a], Jitong Li [a], Gang Yan [b], Rongji Xu [a], Guozhen Xie [a], Xiaoshu Lü[c,d]

[a]Beijing Key Laboratory of Heating, Gas, Ventilation and Air Conditioning, Beijing University of Civil Engineering and Architecture, Beijing 100044, China

[b]Xi'an Jiaotong University, Xi'an, Shanxi 710049, China

[c]Department of Electrical Engineering and Energy Technology, University of Vaasa, P.O.Box 700, FIN-65101 Vaasa, Finland

[d]Department of Civil Engineering, Aalto University, P.O.Box 12100, FIN-02130 Espoo, Finland

Abstract Nanofluids play an essential role in enhancing heat and mass transfer in falling film absorption processes. To reveal the underlying mechanisms of enhanced absorption by nanoparticles at the gas–liquid interface, an innovative model considering the Marangoni effect is proposed for falling film absorption on an inclined plate. The effects of copper oxide nanoparticles on heat and mass transfer for the inclined plate falling film absorption, utilizing lithium bromide solution as the working fluid, are numerically studied using the software COMSOL Multiphysics. The accuracy of the numerical model is verified by experimental and simulation results, showing superior agreement when the Marangoni effect is incorporated. The vapor absorption performance of lithium bromide solution is significantly enhanced by the addition of nanoparticles. Surface tension amplifies temperature and concentration gradients, playing a pivotal role in augmenting heat and mass transfer through the Marangoni effect. The largest temperature and concentration gradients occur at the gas–liquid interface. The interfacial heat transfer coefficient and mass transfer coefficient decrease along the length of the inclined plate and gradually stabilize at 15.01 $W \cdot m^{-2} \cdot K^{-1}$ and 1.12×10^{-4} $m \cdot s^{-1}$, respectively.

Keywords Nanoparticles, nano-LiBr, heat and mass transfer, falling film absorption, Marangoni effect

Nomenclature

A	Area of the mesh, mm^2
C	Mass concentration, %
D	Diffusion coefficient, $m^2 \cdot s^{-1}$
F	Surface tension exerts a volume force on the fluid, N
GCI_{fine}	Convergence index
Gn	Model coefficient of surface tension
H_{abs}	Heat of absorption, $kJ \cdot kg^{-1}$
L	Inclined plate width, m
N	Additive amount, wt.%
NP	Nanoparticle addition amount, wt%
M	The total number of cells used for the computations.
P	The apparent order
Q	Mass flow of solution, $kg \cdot s^{-1}$
R	Mesh convergence ratio
T	Temperature
V	Vapor
a	Liquid film acceleration, $m \cdot s^{-2}$
c_P	Specific heat at constant pressure, $J \cdot kg^{-1} \cdot K^{-1}$
e_a	Relative error
g	Gravitational acceleration, $m \cdot s^{-1}$
h	Relative mesh size
i	Absorbs heat, $kJ \cdot kg^{-1}$
k_h	Heat transfer coefficient, $W \cdot m^{-2} \cdot K^{-1}$
k_m	Mass transfer coefficient, $m \cdot s^{-1}$
$\vec{n}$	Interface normal vector
p	Pressure, kPa
r	Grid refinement factor
q_h	Heat transfer flux, $W \cdot m^{-2}$
q_m	Mass transfer flux, $kg \cdot m^{-2} \cdot s^{-1}$
u	The velocity component in the x direction
v	The velocity component in the y direction
Greek symbol	
Γ	Flow rate of liquid film around unit wetting, $kg \cdot m^{-1} \cdot s^{-1}$
Δ	Dimensionless liquid film thickness
α	Solution concentration, wt%
δ	Falling film thickness, m
ε	The difference between the values of the coarse and fine grids
θ	The tilt Angle of the inclined plate, °

ξ	Solution outlet concentration, %
ρ	Density, $kg \cdot m^{-3}$
σ	Surface tension, $N \cdot m^{-1}$
φ	Simulation value
φ_{ext}	Extrapolated number
	Difference value

Subscripts

a	Approximate
df	LiBr with dispersant
ext	Extrapolated
f	fluid
fine	Fine-grid
I	Liquid bulk region
in	Inlet
n	Normal direction
nf	Nanofluids
o	Initial value
P	Nanoparticles
s	The Sth mesh
t	Tangential direction
v	Vapor
vf	Interface
w	Wall surface

1. Introduction

The utilization of absorption heat pump with sources of low-grade industrial waste heat and solar energy offers an efficient means to efficiently harness the energy and reduce carbon emissions in both industry and building sectors [1], [2], [3]. However, the low thermodynamic performance and large size of the absorption heat pump have become the bottleneck limiting its development [4]. An essential component within this system is the absorber [5], [6], which significantly influences the heat pump's overall performance [7]. Enhancing the absorption characteristics is crucial for improving heat pump efficiency [8]. Nanofluids, known for enhancing heat and mass transfer properties [9], [10], have been selected to improve absorber absorption properties [11], [12]. In the context of falling film absorption, a dominant heat and mass transfer process, the introduction of nanoparticles into the solution has been shown to significantly enhance transfer characteristics [13], [14], [15].

Choi and Kim [13] discovered that adding nanoparticles could increase the heat transfer rate of the radiator with nanofluids by up to 6.9 %. Kim et al. [14] conducted experimental research on the impact of varied amounts of Silicon Dioxide (SiO_2) nanoparticles in falling film absorption of LiBr. The outcomes demonstrated a 46.8 % increase in heat transfer rate and an 18 % increase in mass transfer rate with an addition of 0.005 vol% SiO_2 nanoparticles. Zhang et al. [15] studied the effect of Copper (Cu), Aluminum Trioxide (Al_2O_3), and Carbon Nanotubes (CNT) nanoparticles on the falling film absorption process of LiBr. Results indicated that nanoparticles notably enhanced the absorption process, with Cu nanoparticles showing the highest enhancement effect. Some researchers proposed that the nanoparticle-induced enhancement in thermal conductivity [16], coupled with Brownian motion and micro convection in nanofluids, played key roles in boosting heat and mass transfer during falling film absorption processes [17], [18], [19]. Simultaneously, these nanoparticles in the solution tend to aggregate at the surface of the liquid film, diminishing surface tension and triggering the Marangoni effect [20]. Although nanoparticles can effectively enhance the heat and mass transfer capabilities of falling film absorption, there are some limitations in the experimental research, which fails to elucidate the underlying mechanism.

To address this knowledge gap, some researchers analyzed the effect of nanoparticles on heat and mass transfer in falling film absorption by numerical simulation [21], [22], [23]. Yang et al. [21] investigated the falling film absorption of ammonia water with nanoparticles and dispersants through numerical simulations, considering changes in falling film thickness and physical properties. They examined how the physical properties of nanofluids affect the falling film absorption process. Their findings indicated that the thermal conductivity of nanoparticles influenced the absorption process, whilst nanoparticle viscosity had the most significant effect. The absorption rate of the falling film decreased with increasing nanofluid viscosity. Higher nanofluid mass transfer coefficients were associated with increased absorption rates. Moghadassi et al. [22] conducted numerical investigations into external absorption in horizontal circular tubes and analyzed the impact of Al_2O_3 and Al_2O_3-Cu mixed nanoparticles on heat transfer. They compared the two-phase mixed model with the single-phase model. Results indicated that, according to the single-phase model, the Nusselt number (Nu) for mixed nanofluids increased by 4.73 % for mixed nanofluids when compared to Al_2O_3/H_2O. Moreover, the accuracy of the two-phase hybrid model demonstrated superior accuracy compared to the single-phase model. Zhang et al. [23] incorporated the influences of molecular diffusion and convective diffusion into a mathematical model for the LiBr absorption process within falling films. They investigated the impact of iron tetroxide (Fe_3O_4) nanoparticles on the heat and mass transfer during LiBr falling film absorption. Results indicated enhanced heat and mass transfer, with the degree of enhancement being directly proportional to higher nanoparticle concentration and smaller nanoparticle sizes. Hamida et al. [24] concentrated on the impact of Cu nanoparticles on heat and mass transfer during falling film absorption, disregarding the Soret and Dufour effects. They observed

enhanced heat and mass transfer as nanoparticle quantities increased. However, higher solution inlet concentrations and temperatures constrained the nanoparticle-strengthening effect. Gao et al. [25] established a falling film absorption model for $LiBr/H_2O$, accounting for changes in solution properties and the cooling water channel and tube wall thickness. They studied the influence of adding Copper Oxide (CuO) nanoparticles on falling film absorption performance. Results indicated that the enhancement effect of nano-CuO was more pronounced at higher inlet solution temperatures and lower inlet solution concentrations. Zhou et al [26] developed a mathematical model based on a falling film absorber with ammonia solution to describe the enhancement of nanoparticles accurately. The results indicated that the addition of nanoparticles significantly improved the absorption process in the falling film. And compared with the solution without nanoparticles, the thermal and mass transfer efficiencies increased from 0.385 and 0.443 to 0.523 and 0.600, respectively. Hu [27] simulated the distribution of mass flow rate and heat flow rate at the gas–liquid interface during ammonia nanofluid falling film absorption, investigating the mechanism underlying enhanced absorption due to nanoparticles. The results showed that the heat and mass transfer at the gas–liquid interface was mainly determined by the diffusion term. The enhancement of film absorption was attributed to the Marangoni effect, which arose from the destabilization of interfacial surface tension by the presence of nanoparticles.

In summary, these studies have shown that nanoparticles could effectively strengthen the heat and mass transfer of falling film absorption and Soret and Dufour effects had little impact on falling film absorption process. Further, according to Hu's research [27], the Marangoni effect occurred in the change of the surface tension of the gas–liquid interface, contributing to the enhancement of the heat and mass transfer of falling film absorption. Zhang et al [28] confirmed the existence of the Marangoni effect in gas–liquid films in aqueous ethanol-NaCl solutions. Hu et al. [29] investigated Marangoni boiling experiments on a single component fluid (water), a conventional binary fluid (5 wt% ethanol aqueous solution), and a self-rewetting fluid (5 wt% butanol aqueous solution). The results confirmed that the Marangoni effect, due to the surface tension gradient, was the key to fluid heat transfer enhancement. Li et al [30] developed a theoretical model describing the evaporation kinetics of binary mixture droplets (ethanol–water) by considering the influence of the Marangoni effect, and simulated the kinetics of binary droplets on a heated substrate using a cylindrical coordinate system. The results showed that the temperature difference and ethanol concentration were the main factors affecting the flow and mass transfer of the binary mixture droplets. However, the existing models do not reveal the mechanism by which the Marangoni effect affects solution heat and mass transfer. Enhancing the performance of absorption heat pumps has remained a focal point within the industry. To alter the performance characteristics of absorption heat pumps and enhance the solution absorption capacity, this study employs a novel approach by introducing nanoparticles into lithium bromide solution for falling film absorption while considering the Marangoni effect at the gas–liquid interface. The incorporation of

nanoparticles strengthens the absorption capacity of lithium bromide solution for water vapor. This technique holds significant applied value in altering the operational characteristics of absorption heat pump units and enhancing heat transfer efficiency.

2. Mathematical model

2.1 Physical Model

The inclined plate falling film absorber is shown in Fig. 1**(a)**. Employing an overflow design, the absorber evenly distributes the concentrated solution along the film after it fills the overflow tank. With a length of 480 mm and inclined at an angle of 37° to the horizontal plane, the inclined plate is partitioned into three smaller plates by two dam plates, each 92 mm wide. The quantity of inclined plates utilized is contingent upon the heat and mass transfer load in the experiment.

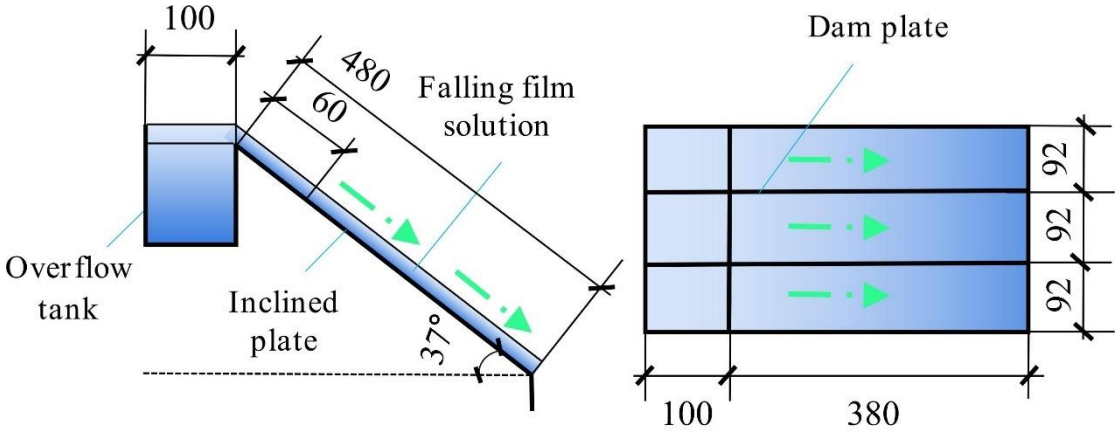

(a) Falling film absorber of an inclined plate (unit: mm).

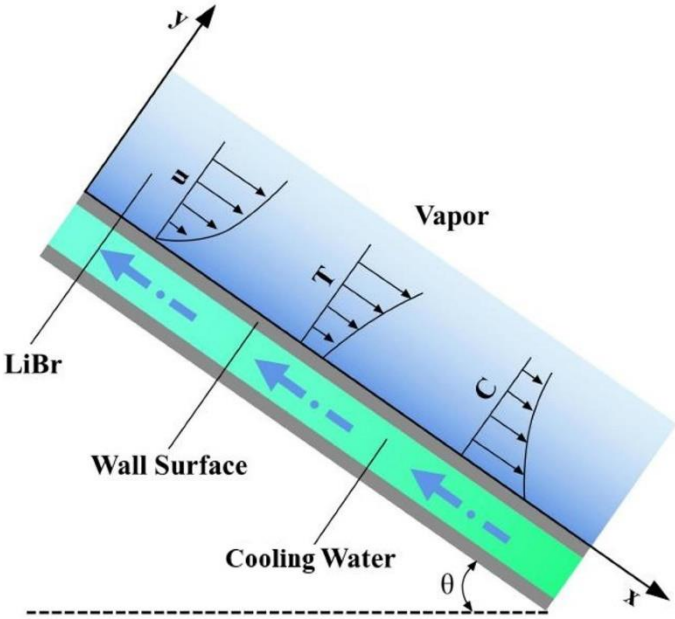

(b) Schematic of absorption process.

Fig. 1. Physical model for falling film absorption on an inclined plate.

In this setup, nano-lithium bromide solution (LiBr) flows down along the inclined plate in a film shape under gravity, making full contact with the vapor on the upper part of the inclined plate. At the gas–liquid interface, water vapor is absorbed by the LiBr, undergoing a phase change from the gas phase to the liquid phase. The latent heat released by water vapor increases the interface temperature, and subsequently, heat is transferred from the gas–liquid interface to the liquid bulk region. To prevent an increase in the temperature of the solution which could result in a decrease in absorption capacity, cooling water is circulated beneath the inclined plate to carry away the absorption heat from the solution. The physical model for the falling film absorption on an inclined plate is illustrated in Fig. 1.

2.2 Basic Assumptions

As shown in Fig. 1**(b)**, the liquid film flows along the X-axis, and the Y-axis represents the thickness direction. The modeling assumptions are as follows.

(1) The surface of the inclined plate is smooth, and the flow is fully developed laminar flow.

(2) The mass flow rate of the solution is constant.

(3) Water vapor flows to the liquid side through the gas-liquid interface, and the surface tension at the interface produces a volume force on the fluid flow.

(4) The gas pressure is constant without mass transfer resistance.

(5) The gas -liquid interface is in equilibrium at the initial state.

(6) The wall of the falling film inclined panel is defined as the boundary condition of constant wall temperature.

(7) Heat transfer in the gas phase is neglected. Heat conduction and mass diffusion along the flow direction are not considered.

(8) The Soret effect and the Dufour effect due to the uneven temperature and concentration fields are ignored.

2.3 Governing Equations and Boundary Conditions

The following governing equations can be obtained for the falling film absorption process of inclined plate based on the above assumptions and the principle of mass, momentum, and energy conservation, expressed by the following formulas:

$$\frac{\partial u}{\partial x}+\frac{\partial v}{\partial y}=0 \tag{1}$$

$$\rho_{nf}\left(u\frac{\partial u}{\partial x}+v\frac{\partial u}{\partial y}\right)=\rho_{nf}g\,sin\,\theta-\frac{\partial p}{\partial x}+\mu_{nf}\left(\frac{\partial^2 u}{\partial x^2}+\frac{\partial^2 u}{\partial y^2}\right)+\frac{\partial F_t}{\partial x} \tag{2}$$

$$\rho_{nf}\left(u\frac{\partial v}{\partial x}+v\frac{\partial v}{\partial y}\right)=\rho_{nf}g\,cos\,\theta-\frac{\partial p}{\partial y}+\mu_{nf}\left(\frac{\partial^2 v}{\partial x^2}+\frac{\partial^2 v}{\partial y^2}\right)+\frac{\partial F_n}{\partial y} \tag{3}$$

$$\rho_{nf} c_P \left(u\frac{\partial t}{\partial x} + v\frac{\partial t}{\partial y}\right) = \lambda_{nf}\left(\frac{\partial^2 T}{\partial x^2} + \frac{\partial^2 T}{\partial y^2}\right) + \frac{\partial(q_m \cdot H_{abs})}{\partial y} \quad (4)$$

$$u\frac{\partial C}{\partial x} + v\frac{\partial C}{\partial y} = D_{nf}\left(\frac{\partial^2 C}{\partial x^2} + \frac{\partial^2 C}{\partial y^2}\right) \quad (5)$$

Where ρ_{nf} represents density of nanofluids, kg·m^{-3}. μ_{nf} represents velocity of nanofluids, Pa·s. g represents gravitational acceleration, m·s^{-2}. λ_{nf} apparent thermal conductivity of nanofluid, W·m^{-1}·K^{-1}. c_p represents specific heat at constant pressure, J·kg^{-1}·K^{-1}. q_m represents mass transfer flux, kg·m^{-2}·s^{-1}. H_{abs} represents heat of absorption, kJ·kg^{-1}. D_{nf} represents the diffusion coefficient of nanofluids, m^2·s^{-1}.

The boundary conditions are shown in Fig. 2.

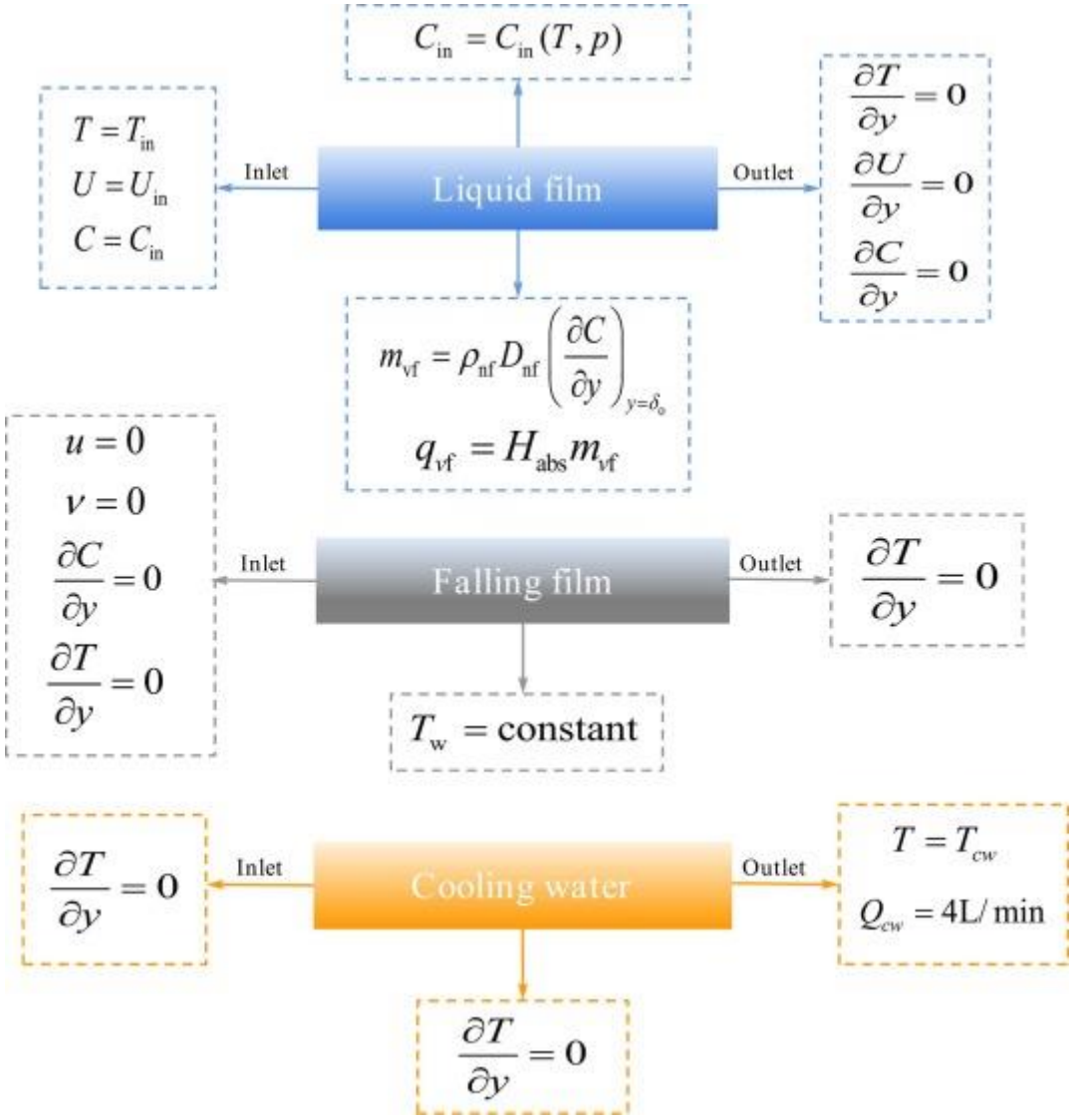

Fig. 2. Boundary conditions.

The boundary conditions are as follows.

（1）At the solution inlet, the temperature, flow rate, and concentration of the liquid film are uniformly distributed.

$$t = t_{in}, v = v_{in}, C = C_{in} \quad (6)$$

Where U represents velocity, m·s^{-1}. u represents the velocity component in the x direction, m·s^{-1}.v represents the velocity component in the y direction, m·s^{-1}.

（2）The solution outlet is the fully developed boundary.

$$\frac{\partial t}{\partial y} = 0, \quad \frac{\partial v}{\partial y} = 0, \quad \frac{\partial C}{\partial y} = 0 \quad (7)$$

（3）The falling film wall has no slip and no seepage, $u = 0, v = 0, \frac{\partial C}{\partial y} = 0$.The falling film wall satisfies the third type of boundary condition, T_w= constant.

（4）At the initial interface, the gas-liquid interface phase is in equilibrium，$C_{in} = C_{in}(t, p)$.

（5）Mass transfer energy at the gas-liquid interface，$m_{vf} =$ $\rho_{nf} D_{nf} \left(\frac{\partial C}{\partial y}\right)_{y=\delta_o}$ .Thermal energy at the gas-liquid interface，$q_{vf} = H_{abs} m_{vf}$.

2.4 Model Parameters and Operating Conditions

(1) Momentum source term

The nano-LiBr flows down the inclined plate to form a thin film, the vapor enters the main liquid bulk region through the gas-liquid interface and is absorbed by the solution. The addition of nanoparticles introduces extra forces due to the surface tension caused by the concentration gradient at the interface. According to the divergence theorem, the surface tension at the interface exerts a volume force on the fluid, serving as a source term in the momentum equation. According to the continuous surface force (CSF) model [29], the force exerted by surface tension at the gas-liquid interface on the solution can be divided into normal interface force F_n and tangential interface force F_t along the interface's direction [30], expressed by the following formula:

$$F_n = \sigma \frac{\rho\gamma}{\frac{1}{2}(\rho_v + \rho_L)} \cdot \left(\frac{\partial \xi_w}{\partial y} + \frac{\partial \xi_w}{\partial y}\right) \quad (8)$$

where

$$\gamma = \frac{\partial \vec{n}}{\partial x} + \frac{\partial \vec{n}}{\partial y} \quad (9)$$

$$\vec{n} = \frac{\frac{\partial \xi_w}{\partial x} + \frac{\partial \xi_w}{\partial y}}{\left|\frac{\partial \xi_w}{\partial x} + \frac{\partial \xi_w}{\partial y}\right|} \quad (10)$$

and

$$F_t = \left[\vec{n} \times \left(\frac{\partial \sigma}{\partial x} + \frac{\partial \sigma}{\partial y}\right)\right] \times$$

$\vec{n}$ (11)

Disregarding the impact of dispersants and added nanoparticles on the surface tension of nano-LiBr, the surface tension of nano-LiBr is calculated as a function of solution concentration and temperature.

$$\frac{\partial \sigma}{\partial x}+\frac{\partial \sigma}{\partial y}=\frac{\partial \sigma}{\partial \xi_w}\left(\frac{\partial \xi_w}{\partial x}+\frac{\partial \xi_w}{\partial y}\right)+\frac{\partial \sigma}{\partial T}\left(\frac{\partial T}{\partial x}+\frac{\partial T}{\partial y}\right) \tag{12}$$

Therefore, the force in the tangential direction of the interface can be expressed as:

$$F_t = \frac{\partial \sigma}{\partial \xi_w}\left[\vec{n}\times\left(\frac{\partial \xi_w}{\partial x}+\frac{\partial \xi_w}{\partial y}\right)\right]\times\vec{n}+\frac{\partial \sigma}{\partial T}\left[\vec{n}\times\left(\frac{\partial T}{\partial x}+\frac{\partial T}{\partial y}\right)\right]\times\vec{n} \tag{13}$$

where

$$\vec{n}=[\cos\theta \ \ sin\theta \ 0] \tag{14}$$

$$\nabla\xi_w=[\frac{\partial \xi_w}{\partial x} \ \frac{\partial \xi_w}{\partial y} \ 0] \tag{15}$$

$$\nabla T=[\frac{\partial T}{\partial x} \ \frac{\partial T}{\partial y} \ 0] \tag{16}$$

The force in the tangential direction of the interface can be obtained as:

$$F^t_{vf,x}=\frac{\partial \sigma}{\partial \xi_w}sin\theta\left(sin\theta\frac{\partial \xi_w}{\partial y}-cos\theta\frac{\partial \xi_w}{\partial y}\right)+\frac{\partial \sigma}{\partial T}sin\theta\left(sin\theta\frac{\partial T}{\partial y}-cos\theta\frac{\partial T}{\partial y}\right) \tag{17}$$

$$F^t_{vf,y}=-\frac{\partial \sigma}{\partial \xi_w}cos\theta\left(sin\theta\frac{\partial \xi_w}{\partial y}-cos\theta\frac{\partial \xi_w}{\partial y}\right)-\frac{\partial \sigma}{\partial T}cos\theta\left(sin\theta\frac{\partial T}{\partial y}-cos\theta\frac{\partial T}{\partial y}\right) \tag{18}$$

(2) Nanofluids properties

Nanofluids properties are taken from the literature, for example, density [31], viscosity [32], specific heat capacity [31], thermal conductivity [33] and surface tension

[34], expressed by the following formulas:

$$\rho_{\mathrm{nf}} = (1-N_{\mathrm{P}})\rho_{\mathrm{f}} + N_{\mathrm{P}}\rho_{\mathrm{p}} \tag{19}$$

$$\mu_{\mathrm{nf}} = \frac{\mu_{\mathrm{f}}}{(1-\mathrm{N})^{2.5}} \tag{20}$$

$$D_{\mathrm{nf}} = \frac{\kappa T}{6\pi \mathrm{r}\mu_{\mathrm{nf}}} \tag{21}$$

$$(C_{\mathrm{p}})_{\mathrm{nf}} = (1-\mathrm{N})(C_{\mathrm{p}})_{\mathrm{f}} + \mathrm{N}(C_{\mathrm{p}})_{\mathrm{P}} \tag{22}$$

$$\frac{k_{\mathrm{nf}}}{k_{\mathrm{f}}} = \frac{k_{\mathrm{P}} + 2k_{\mathrm{f}} - 2\,\mathrm{N}(k_{\mathrm{f}} - k_{\mathrm{P}})}{k_{\mathrm{P}} + 2k_{\mathrm{f}} + \mathrm{N}(k_{\mathrm{f}} - k_{\mathrm{P}})} \tag{23}$$

$$\frac{\sigma_{nf}}{\sigma_{df}} = \left(\sum_0^4 \mathrm{F_n}\,\mathrm{N_P} + \left(\alpha - \frac{1}{2}\right)\sum_0^4 \mathrm{G_n}\,\mathrm{N_P}\right) \tag{24}$$

(3) Other parameters

Other parameters include the thickness of the falling film, interfacial heat transfer flux, interfacial heat transfer coefficient, interfacial mass transfer flux, and interfacial mass transfer coefficient.

The thickness of the falling film of the nano-LiBr:

$$\delta_{nf} = \left(\frac{3\Gamma\mu_{nf}}{\rho_{nf}^2 a}\right)^{\frac{1}{3}} \tag{25}$$

where

$$a = g\sin\theta \tag{26}$$

$$\Gamma = \frac{Q_{nf}}{L} \tag{27}$$

The adopted dimensionless liquid film thickness is defined as:

$$\Delta = \frac{y}{\delta_{nf}} \tag{28}$$

The interfacial parameters are expressed as:

$$q_h = k_h\left(\frac{\partial T}{\partial y}\right)_{y=\delta_{nf}} - (c_{nf} - c_v)\mathrm{T}\rho_{nf}D_{nf}\left(\frac{\partial T}{\partial y}\right)_{y=\delta_{nf}} \tag{29}$$

$$k_h = \frac{q_h}{T_i - T_w} \tag{30}$$

$$q_m = -\rho_{nf}D_{nf}\left(\frac{\partial \xi_w}{\partial y}\right)_{y=\delta_{nf}} \tag{31}$$

$$k_m = \frac{\dot{M}(x)}{\rho_{nf,i} S \triangle \xi_w(x)} \quad (32)$$

where q_h represents heat transfer flux with heat transfer coefficient, W·m^{-2}. k_h represents heat transfer coefficient, W·m^{-2}·K^{-1}; q_m represents mass transfer flux, kg·m^{-2}·s^{-1}. and k_m represents mass transfer coefficient, m·s^{-1}.

(4) Operating conditions

The operating conditions are displayed in Table 1. In this study, the inlet temperature of the falling film solution (313.15 K), the solution concentration (58 %), the flow rate of the falling film solution (0.2 ~ 1.0 L/min), the inlet temperature of the cooling water (298.15 K) and the flow rate (4 L/min) of the cooling water were selected based on the absorption heat pump operating conditions. The amount of nanoparticles added (0 to 0.15 wt%), the density of nanofluid (1669.92 kg/m^3), the viscosity of nanofluid (4.443E-3 Pa·s) and the thermal conductivity of nanofluid (26.1439 W/(m·K)) were determined experimentally [17].

Table 1 Operating Conditions

Parameter	Parameter value
Solution inlet concentration (%)	58
Solution inlet temperature (K)	313.15
Solution flow (L/min)	0.2~1.0
Cooling water inlet temperature (K)	298.15
Cooling water flow (L/min)	4
absorb pressure (kPa)	1.2
Inclined plate length (mm)	480
Slope width (mm)	276
Amount of nanoparticles added (wt.%)	0~0.15
Amount of dispersant added (wt.%)	2
Nanofluid Density (kg/m^3)	1669.92
Nanofluid viscosity (Pa·s)	4.443E-3
Thermal conductivity of nanofluids (W/(m·K))	26.1439
Nanofluid diffusivity (m^2/s)	8.34864E-10

3. Numerical procedure

3.1 Meshing and Independence Verification

In this research, the laminar flow and heat and mass transfer modules in the COMSOL Multiphysics software are selected to establish a falling film absorption model of nano-LiBr for the sloping plate of 480 mm length. The PAEDISO solver for

steady-state simulations and a multi-threaded nested dissection preordering algorithm are utilized for solving. A structured quadrilateral mesh compatible with the calculation area is used in the model. The mesh configuration of the falling film is shown in Fig. 3.

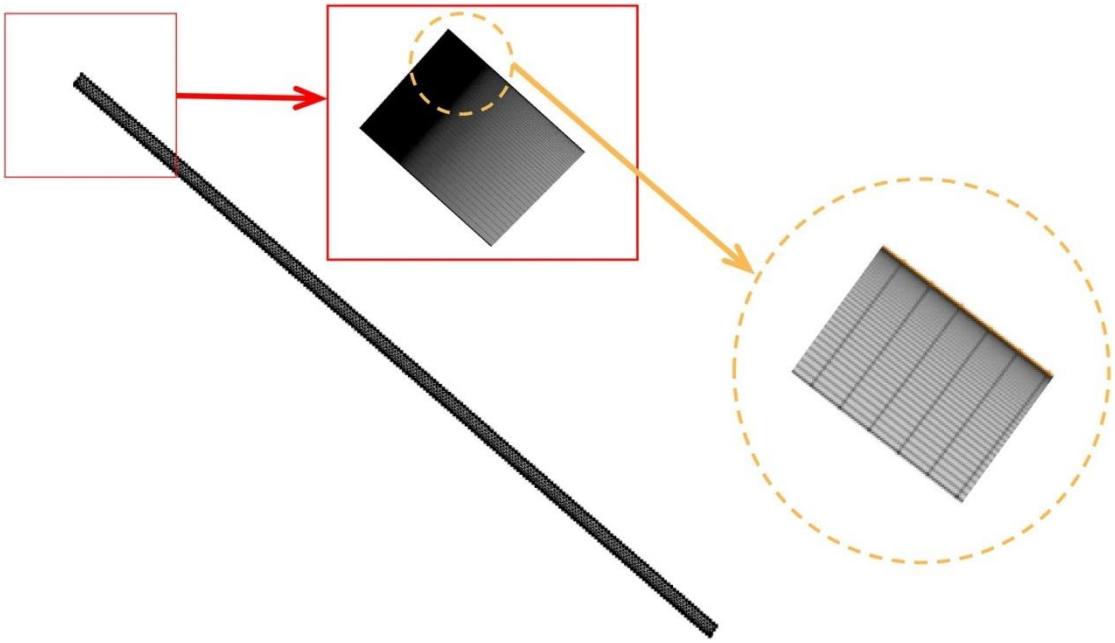

Fig. 3. Mesh configuration of the falling film.

As shown in **Table 2**, the grid is encrypted in both the horizontal and vertical directions respectively, and three different grids (48000, 96000, and 192000) are used to evaluate the grid convergence based on the convergence ratio of grids.

$$R=\frac{\varepsilon_{21}}{\varepsilon_{32}} \tag{32}$$

where

$$\varepsilon_{21}=\varphi_2-\varphi_1 \tag{33}$$

$$\varepsilon_{32}=\varphi_3-\varphi_2 \tag{34}$$

$$r_{21} = \frac{hm\ s_2}{hm\ s_1} \tag{38}$$

$$r_{32} = \frac{hm\ s_3}{hm\ s_2} \tag{39}$$

$$hms = \left[\frac{1}{M}\sum_{S=1}^{M}(\Delta A_s)\right]^{\frac{1}{2}} \tag{40}$$

$$\frac{\varepsilon_{32}}{r_{32}^{p}-1} = \frac{\varepsilon_{21} r_{21}^{r}}{r_{21}^{p}-1} \tag{41}$$

$$e_a^{21} = \left|\frac{\varphi_1-\varphi_2}{\varphi_1}\right| \tag{42}$$

$$GCI_{fine}^{21} = \frac{1.25 e_a^{21}}{r_{21}^{r}-1} \tag{43}$$

$$\varphi_{ext}^{21} = \frac{r_{21}^{r}\varphi_1-\varphi_2}{r_{21}^{r}-1} \tag{44}$$

$$e_{ext}^{21} = \left|\frac{\varphi_{ext}^{12}-\varphi_1}{\varphi_{ext}^{12}}\right| \tag{45}$$

Table 2. Mesh sensitivity analysis.

Case	ID	Meshes	C_{out}
1	φ_1	1200×40	57.499
2	φ_2	2400×40	57.498
3	φ_3	3600×40	57.496
R	_	–	0.5
4	φ_4	2400×20	57.482
5	φ_5	2400×40	57.498
6	φ_6	2400×60	57.505
R	–	–	0.57

Table 3 shows that for the outlet concentration of the absorber, the numerical

uncertainties in the fine mesh are 0.0019% and 0.0079%, which meet the request for numerical simulation [36]. Therefore, a 2400×40 grid is chosen for a total of 96000.

Table 3 Calculation of grid discretization error of solution outlet concentration.

Item	φ_1 — φ_3	φ_4 — φ_6
r_{21}, r_{54}	1.43	1.43
r_{32}, r_{65}	1.4	1.4
P	2.1	1.7
ϕ_{ext}^{21}, ϕ_{ext}^{54}	57.46	57.47
e_a^{21}, e_a^{54}	0.0017%	0.0070%
e_{ext}^{21}, e_{ext}^{54}	0.068%	0.021%
GCI_{fine}^{21}, GCI_{fine}^{54}	0.0019%	0.0079%

3.2 Model Verification

Under identical operational conditions (with 0.1% CuO addition), a comparison is made between our numerical outcomes, Wang et al.'s experimental findings [17], and the numerical results by Gao et al. [25]. This comparison illustrates the alteration in outlet concentrations during falling film absorption concerning solution flow rates (refer to **Fig. 2**). Our simulation results exhibit a better correspondence with the experiments, with a maximum deviation of 0.3% in the model.

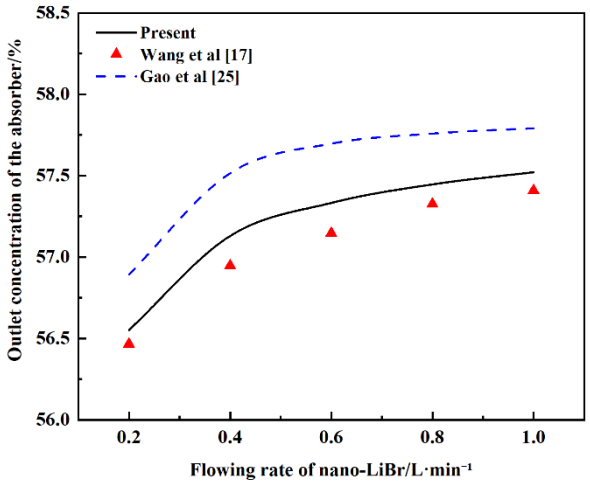

Fig. 4. Comparison between experimental and simulation results.

4. Results and discussion

4.1. Mechanism of heat and mass transfer by falling film absorption

Fig. 5 shows the mechanism through which nanoparticles enhance the heat and mass transfer characteristics of falling film absorption. The Marangoni effect reinforces convection at the gas–liquid interface, enhancing the heat and mass transfer capability for the falling film absorption. Additionally, when water vapor absorbed by the LiBr crosses the gas–liquid interface, the LiBr concentration near the interface on the liquid side is lower than that in the bulk liquid region. Nanoparticles flow to the gas–liquid interface driven by this concentration gradient, subsequently transporting water molecules and absorption heat from the gas–liquid interface to the liquid bulk region. These nanoparticle transport attributes enhance the heat and mass transfer capability of the solution, as shown in Fig. 5**(a)**. Notably, the Marangoni effect exerts the most significant impact on enhancing heat and mass transfer during the falling film absorption process. The presence of Marangoni effect expands the temperature and concentration gradients, which is a significant factor in the enhancement of heat and mass transfer by falling film absorption, as shown in Fig. 5**(b)**.

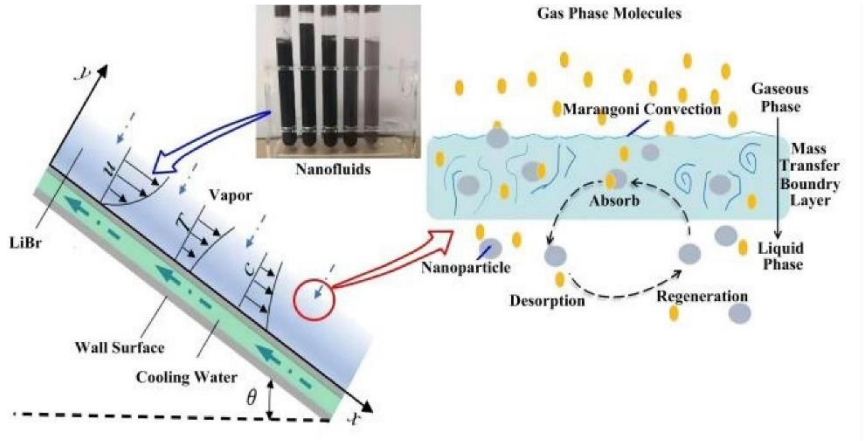

(a) Nanoparticle transport properties

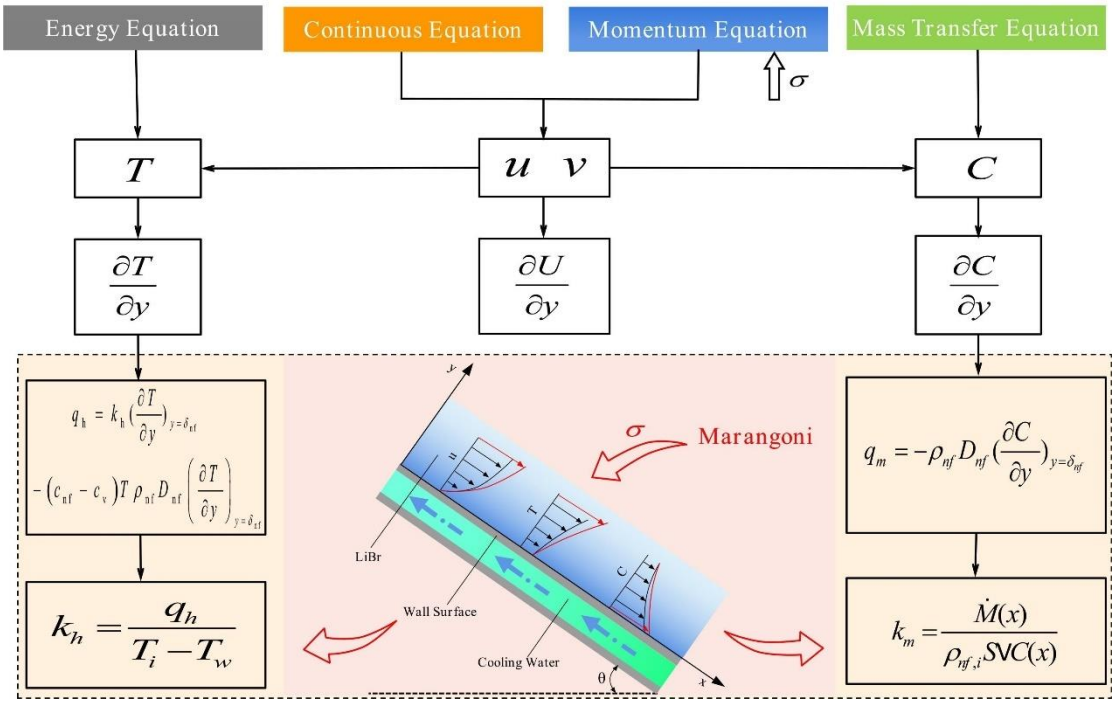

Fig. 5. Schematic of nanoparticles enhanced heat and mass transfer characteristics for falling film absorption.

4.2. Marangoni effect verification

To verify the existence of the Marangoni effect at the interface of the heat mass transfer in falling film absorption, we investigated the velocity, temperature, and concentration fields at the inlet of a falling film absorption. The investigation was conducted under operational conditions involving a 50 % concentration solution, 40 °C inlet temperature, 0.05 m/s inlet flow rate, 20 °C cooling water temperature, 0.4 L/min cooling water flow rate, 0.05 wt% nanoparticle addition, and 2 wt% dispersant addition.

Fig. 6 illustrates the distribution of the velocity field at the inlet of the falling film absorption. Color-coded regions indicate the magnitude of velocity distribution, while the black curves represent the velocity contour. Fig. 6**(a), (b) and (c)** shows the distribution of velocity field for falling film absorption, considering the Marangoni effect and without considering the Marangoni effect, at X = 0 ~ 20 mm, X = 50 ~ 70 mm, and X = 460 ~ 480 mm, respectively. A comparison between the figures reveals that velocity contours within the falling film are notably denser at the gas–liquid interface when accounting for the Marangoni effect. Enhanced velocity gradients exist at the gas–liquid interface, oriented towards it, indicating intensified solution flow at this interface. Consequently, the Marangoni effect intensifies solution flow at the gas–liquid interface, heightening the convection effect, particularly noticeable at the falling film's inlet.

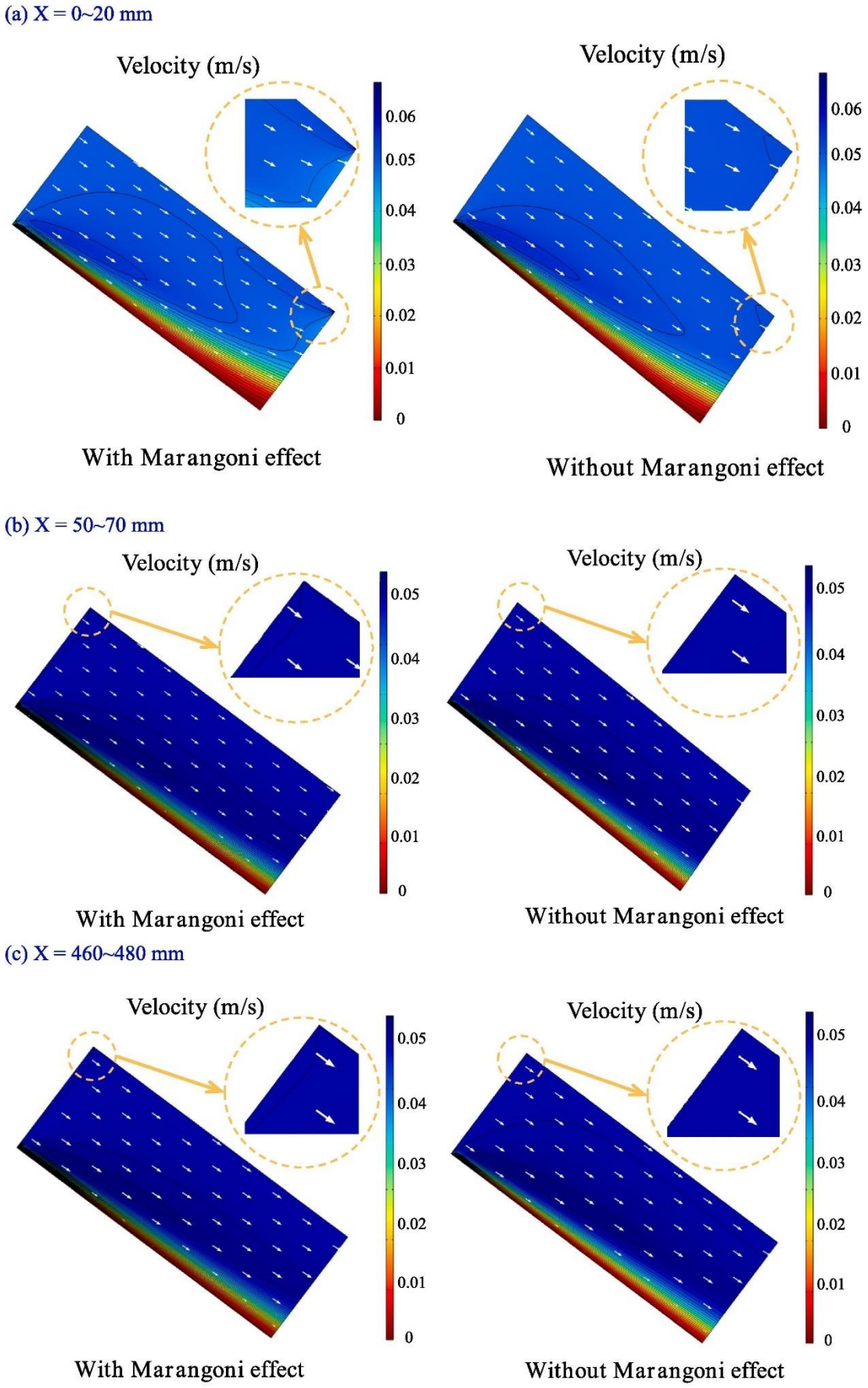

Fig. 6. The velocity field along the length of the falling film.

Fig. 7 shows the temperature field distribution at the inlet of the falling film absorption. Color-coded areas indicate the temperature distribution, while the black curves represent the heat flux contours. Fig. 7**(a), (b) and (c)** shows the temperature distribution for falling film absorption, considering the Marangoni effect and without considering the Marangoni effect, at X = 0 ~ 20 mm, X = 50 ~ 70 mm, and X = 460 ~ 480 mm, respectively. A comparison between the figures shows that incorporating the Marangoni effect at the gas–liquid interface results in denser heat transfer flux contours within the temperature field of the falling film. This leads to heightened heat transfer at the gas–liquid interface. Therefore, the presence of the Marangoni effect intensifies convective heat transfer at the gas–liquid interface, particularly noticeable at the inlet of the falling film absorption.

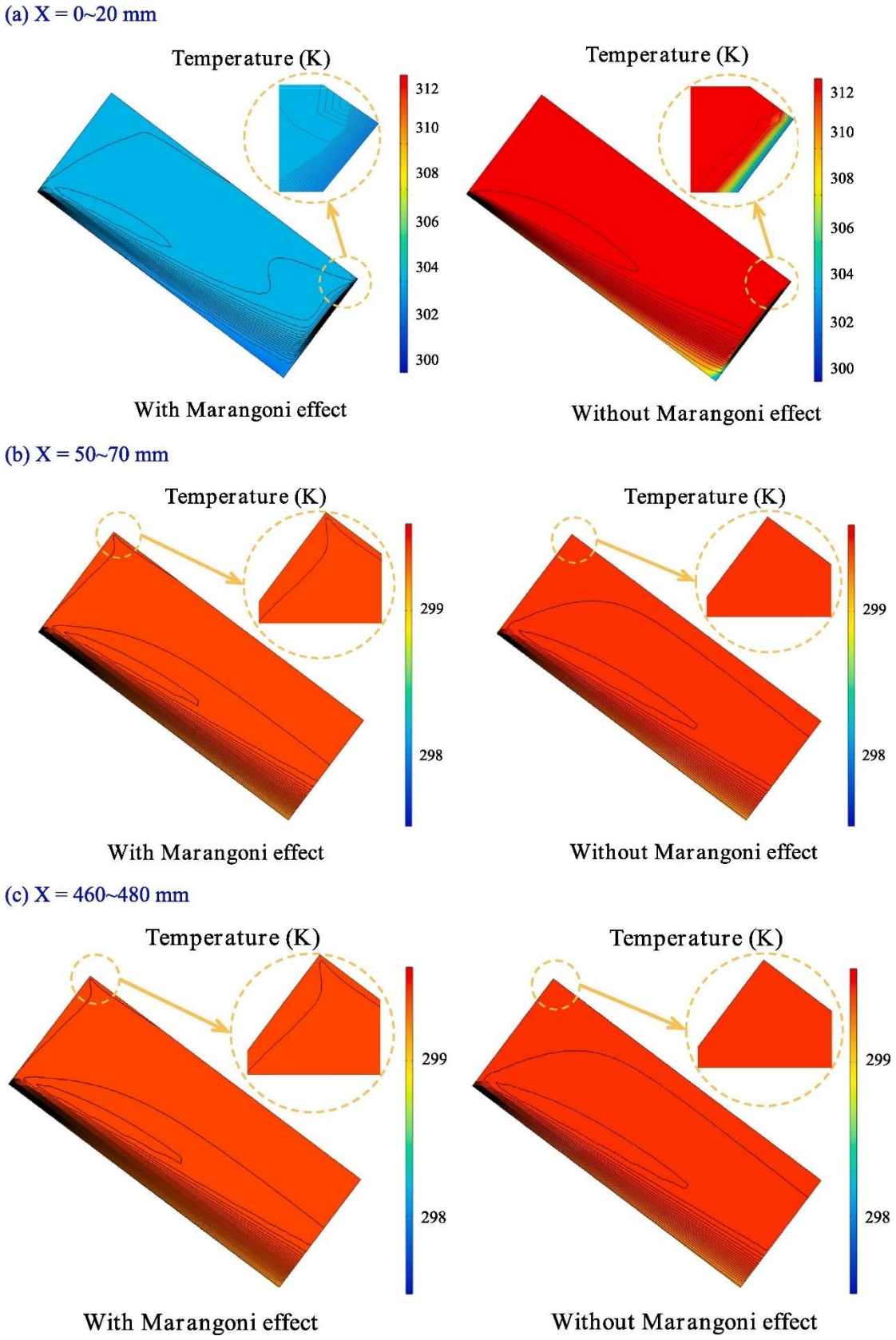

Fig. 7. The temperature field along the length of the falling film.

Fig. 8 shows the concentration field distribution at the inlet for the falling film absorption. Color-coded regions indicate the velocity distribution, while the black curves represent the mass flux contours. Fig. 8**(a), (b) and (c)** the concentration field distribution for falling film absorption, considering the Marangoni effect and without considering the Marangoni effect, at X = 0 ~ 20 mm, X = 50 ~ 70 mm, and X = 460 ~ 480 mm, respectively. Upon comparing the figures, it becomes evident that the inclusion of the Marangoni effect at the gas–liquid interface in the falling film absorber results in denser mass transfer flux contours, indicating heightened mass transfer at the interface. Therefore, the existence of the Marangoni effect enhances the convective diffusion effect at the gas–liquid interface, with a more pronounced impact at the falling film's inlet.

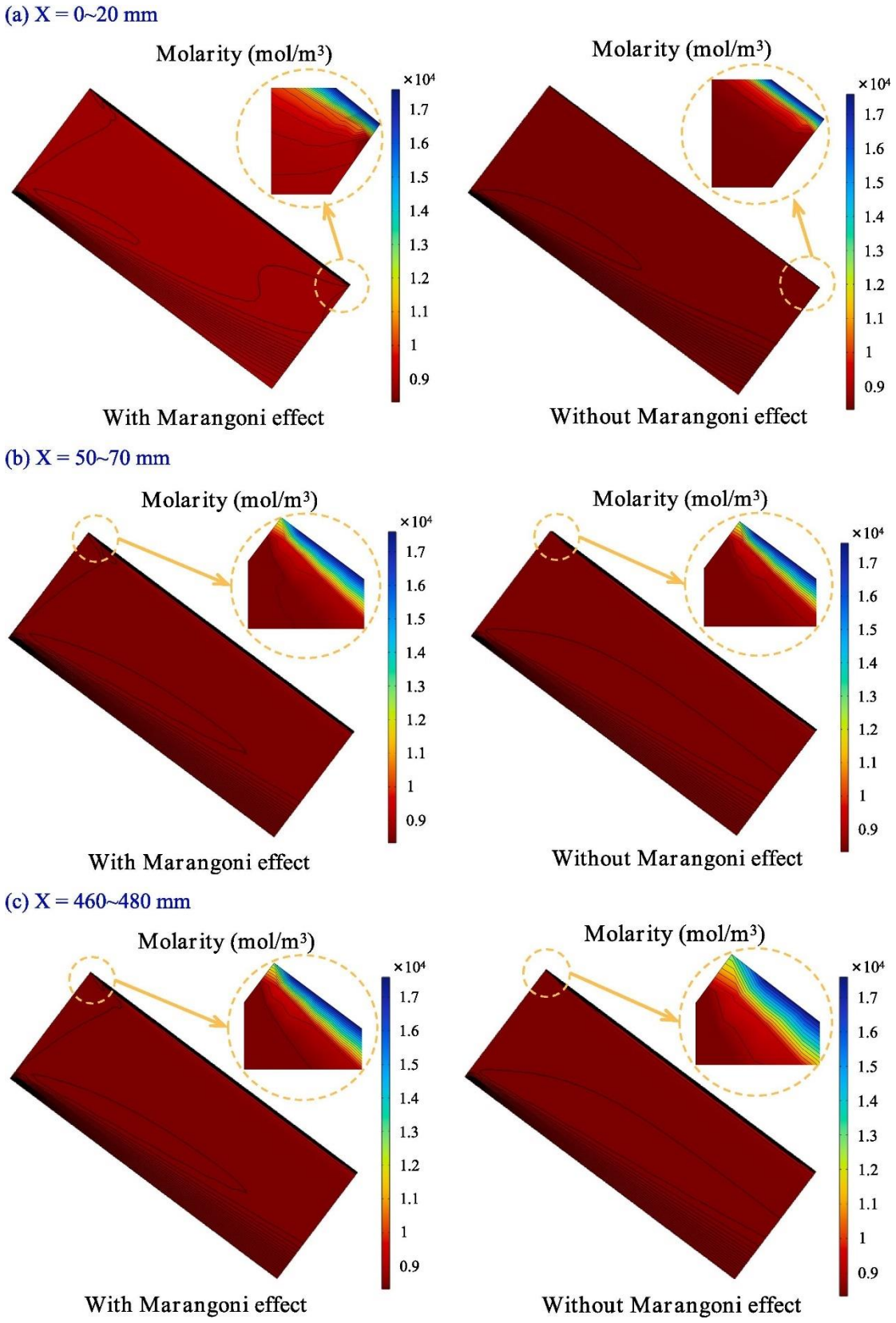

Fig. 8. The concentration field along the length of the falling film.

As shown in Fig. 6, Fig. 7, Fig. 8, the heat and mass transfer within nanoparticle falling film absorption experience enhancement due to the Marangoni effect stemming from the gas–liquid interface and the transport attributes of nanofluids. The nanoparticles near the gas–liquid interface introduce perturbations, resulting in thinning of the liquid film. This change in the liquid film induces a surface tension gradient at the gas–liquid interface, known as the Marangoni effect.

4.3. Distribution of temperature field and concentration field

Fig. 9 shows the temperature distribution of nano-LiBr along the length of the falling film at a flow rate of 1.0 L/min. **In** Fig. 9**(a)** and Fig. 9**(b)**, the temperature of nano-LiBr at both the gas–liquid interface and the main liquid phase region gradually decreases along the inclined plate's length. A rapid temperature drop occurs within the falling film length of 0–40 mm. Subsequently, the temperature continues to decrease along the inclined plate within the range of 40–480 mm. When the nanoparticle mass fraction is 0.15 wt%, the gas–liquid interface temperature of nano-LiBr ranges from 308.89 K to 298.65 K, while the temperature in the main liquid phase area ranges from 303.76 K to 298.64 K.

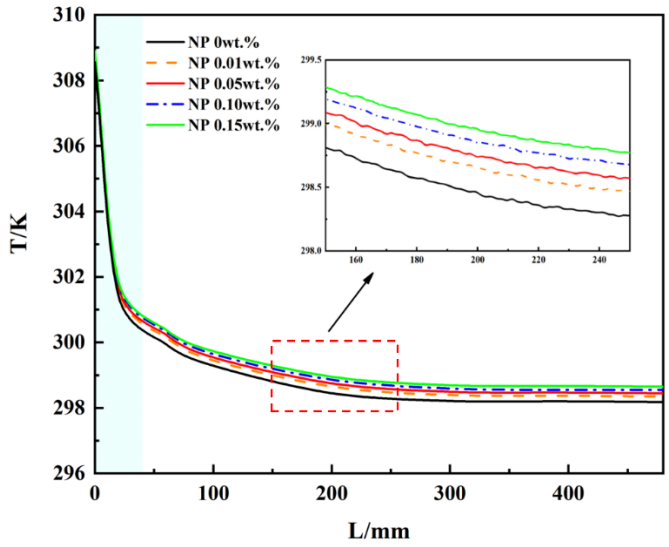

(a) Gas-liquid interface area.

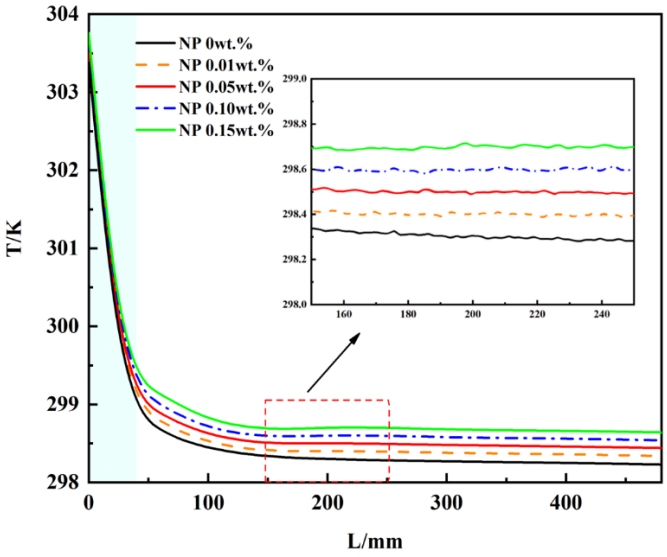

(b) Liquid phase main area.

Fig. 9. Variation of temperature field along the length of the falling film with nanoparticles mass fraction.

The primary reason lies in the elevated inlet concentration of the solution, generating a substantial driving force for mass transfer, leading to a release of significant latent heat upon water vapor absorption. However, as the solution's concentration diminishes, the driving force for mass transfer, the rate of water vapor absorption, and the latent heat released decrease correspondingly. Simultaneously, at a given position on the inclined plate, the introduction of nanoparticles results in temperature elevation. This can be attributed to the micro-disturbance caused by nanoparticles, leading to reduced surface tension at the gas–liquid interface, thereby lowering mass transfer resistance. Additionally, nanoparticles' addition coupled with the presence of the Marangoni effect augment the heat transfer capacity within the liquid phase.

The concentration field distribution of nano-LiBr along the length of the falling film for the flow rate of 1.0 L/min is shown in Fig. 10. In Fig. 10**(a)** and **(b)**, both the gas–liquid interface and the main liquid phase region of nano-LiBr exhibit gradual concentration decline along the inclined plate's length. Notably, the concentration reduction is rapid within the first 0–40 mm length range of the falling film. Subsequently, within the 40–480 mm length range, the reduction rate slows down. With a nanoparticle mass fraction of 0.15 wt%, the gas–liquid interface concentration of nano-LiBr drops from 0.58 % to 0.481 %, and the concentration in the main liquid phase area decreases from 0.58 % to 0.574 %.

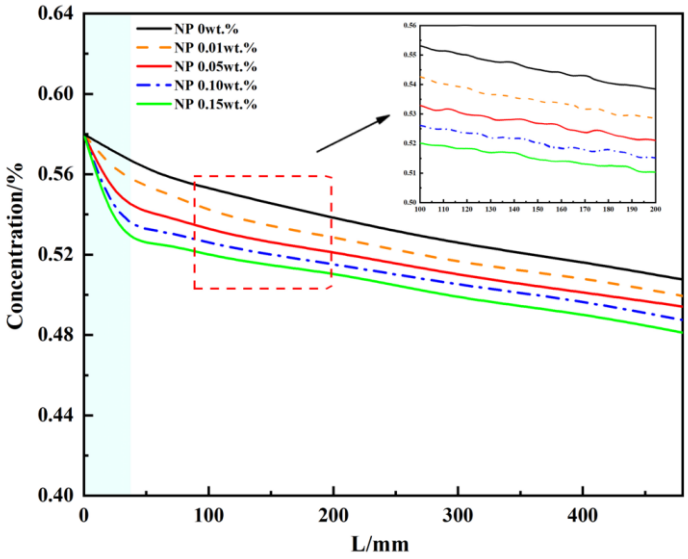

(a) Gas-liquid interface.

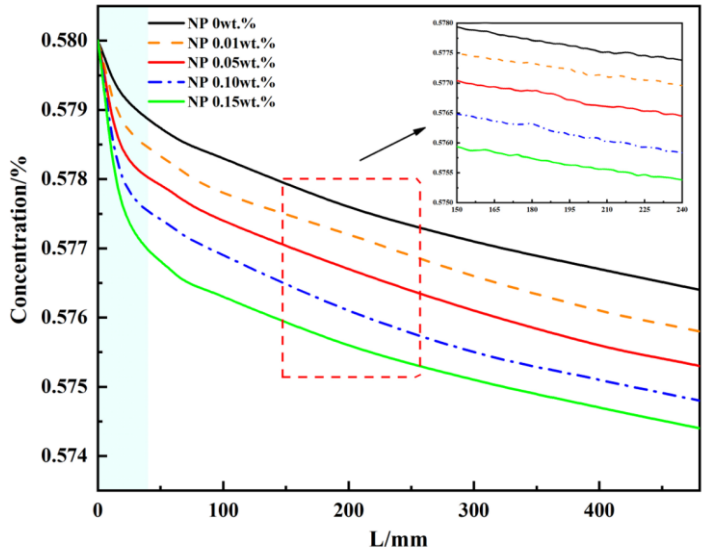

(b) Liquid phase main area.

Fig. 10. Variation of concentration field along the length of the falling film with nanoparticles mass fraction.

The main reason is that the high inlet concentration of the solution, coupled with the saturated vapor pressure of the solution decreasing due to the low-temperature cooling water, leads to a relatively large driving force for the mass transfer. However, as the solution's concentration diminishes along the falling film, both the driving force for mass transfer and the rate of water vapor absorption decrease. Additionally, at a given position on the inclined plate, the presence of nanoparticles causes a reduction in solution concentration. This can be attributed to nanoparticle-induced micro-

perturbations at the gas–liquid interface, which lower surface tension, coupled with the enhancement of mass transfer through the Marangoni effect.
The temperature distribution of nano-LiBr at various positions along the falling film, under a flow rate of 1.0 L/min, is illustrated in Fig. 11. In the direction perpendicular to the liquid film's thickness, the solution temperature progressively rises, reaching its peak at the gas–liquid interface.

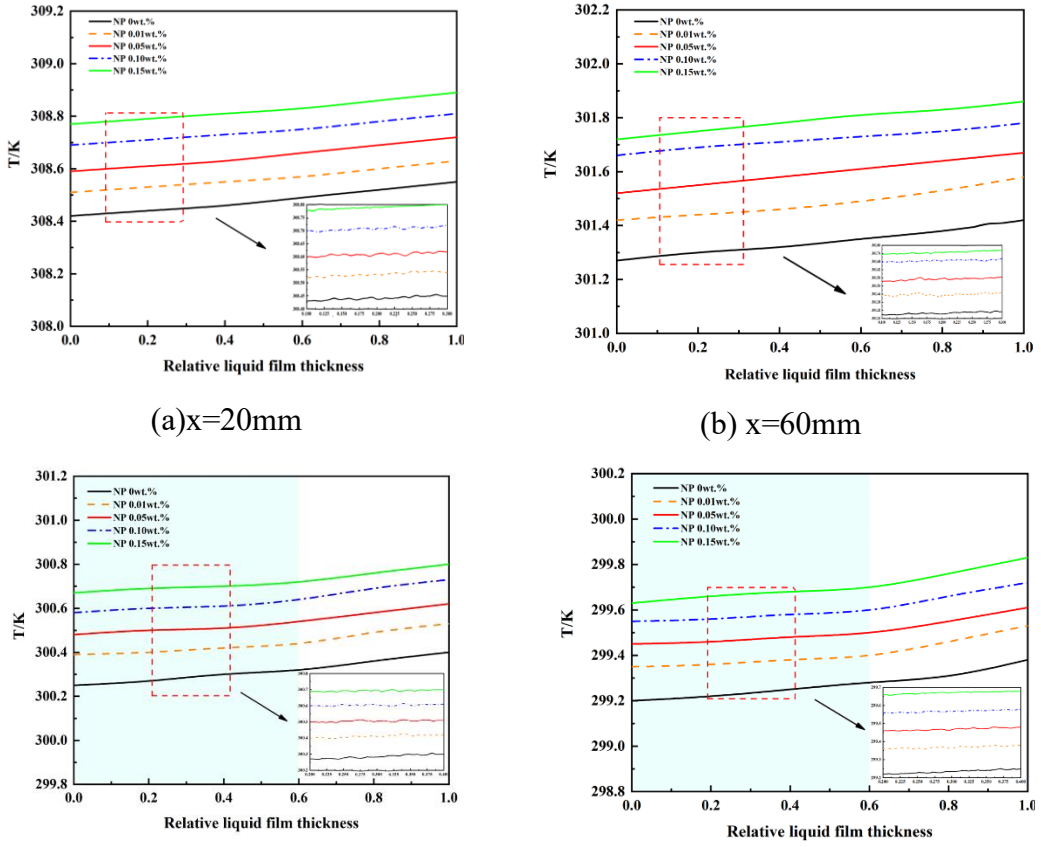

(a)x=20mm (b) x=60mm

(c) x=100mm (d) x=200mm

Fig. 11. Variation of temperature field along the liquid film thickness with nanoparticles mass fraction.

The main reason is that the water vapor at the gas–liquid interface is absorbed by the solution and the latent heat of vaporization is released, which leads to the increase of the temperature at the gas–liquid interface. Under a consistent liquid film thickness, the solution temperature increases with the addition of the nanoparticles. This can be attributed to nanoparticle-induced micro-perturbations that decrease surface tension at the gas–liquid interface, facilitating the entry of water molecules into the liquid phase region. This process augments latent heat release and bolsters heat transport from the gas–liquid interface to the film's wall.
The most significant temperature gradient in the solution occurs at a falling film length of 20 mm. As the solution descends the inclined plate, the temperature gradient within the liquid film gradually diminishes and eventually levels off. This trend is

primarily attributed to the high initial concentration of the incoming solution, leading to rapid water vapor absorption driven by mass transfer. Consequently, the highest amount of latent heat is released during this phase. Furthermore, as the solution continues its descent, the average concentration within the liquid film decreases. This reduction in concentration decreases the mass transfer driving force at the gas–liquid interface, resulting in decreased water vapor absorption and released latent heat. As a consequence, the temperature gradient within the liquid film decreases.

The concentration field distribution of nano-LiBr in the liquid film at different positions along the falling film, with a flow rate of 1.0 L/min, is shown in Fig. 12. The solution's concentration gradient remains stable near the wall while experiencing rapid augmentation near the gas–liquid interface. Notably, the lowest concentration of the solution is observed at the gas–liquid interface.

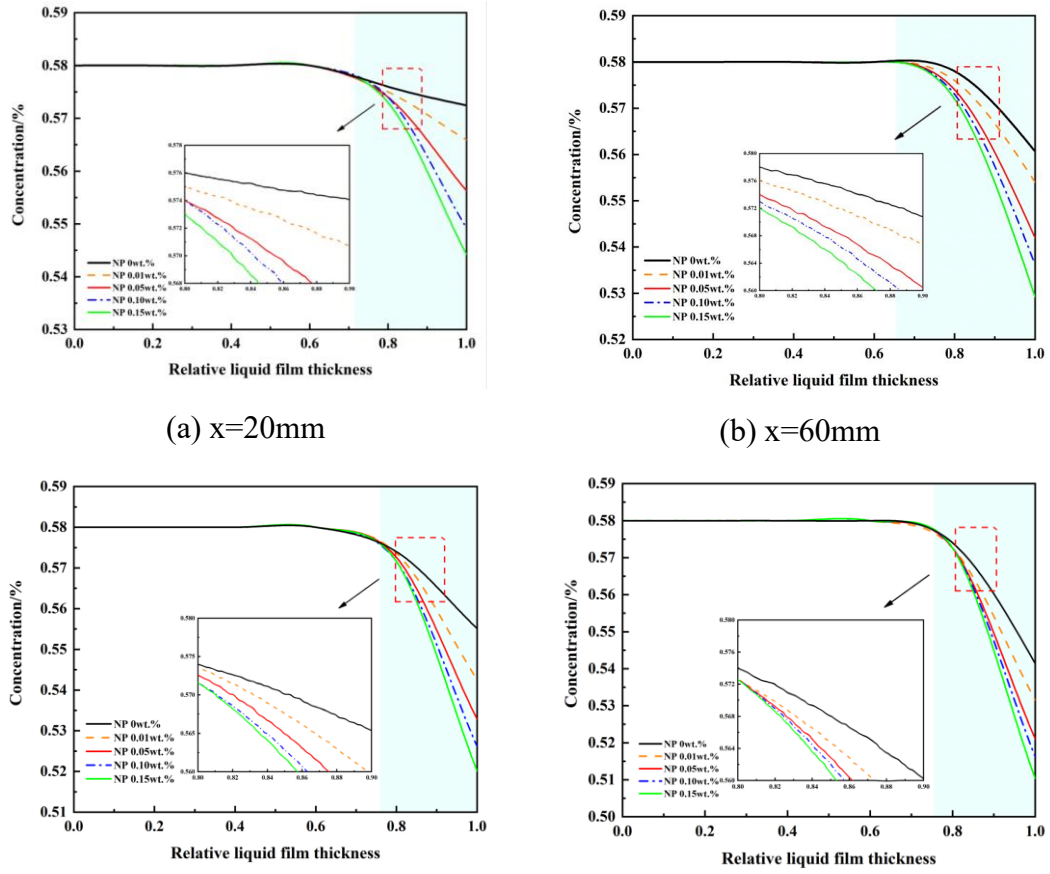

(a) x=20mm (b) x=60mm

(c) x=100mm (d) x=200mm

Fig. 12. Variation of concentration field along the liquid film thickness with nanoparticles mass fraction.

The primary factor is the mass transfer driving force that propels water molecules from the gas phase through the gas–liquid interface and into the liquid phase region through convection and diffusion. This influx of water molecules reduces the solution concentration at the gas–liquid interface, gradually diffusing them into the main liquid phase. With a consistent liquid film thickness, the solution's concentration diminishes

progressively with the introduction of nanoparticles. The main reason is nanoparticles' micro-perturbation and transport properties, which amplify the gas–liquid interface's diffusion capacity into the liquid bulk region, thereby reducing mass transfer resistance. Additionally, the Marangoni effect generated by the gas–liquid interface intensifies convection, enhancing the heat and mass transfer capabilities of falling film absorption.

It can be seen from Figs. 11 and 12 that the temperature field and the concentration field have opposite transfer directions. The temperature field is transferred from the gas–liquid interface direction to the wall direction, while the concentration field follows the opposite direction. Along the liquid film thickness at the same falling film position, the temperature boundary layer initiates its movement prior to the concentration boundary layer. This is primarily due to the superior heat diffusion ability in the solution compared to the mass diffusion ability of water molecules in the solution.
In the direction of liquid film thickness at the same falling film position, nanoparticles accelerate the movement of the temperature boundary layer towards the wall and the solution concentration boundary layer towards the gas–liquid interface. Nevertheless, the driving force for mass transfer weakens with the temperature at the gas–liquid interface. As a result, changes in the concentration field during the vapor absorption mass transfer process of nano-LiBr are influenced by variations in the temperature field. The interplay between the temperature and concentration fields must not be disregarded.

4.4. Heat transfer

As shown in Fig. 13, at a flow rate of 1.0 L/min, the heat transfer flux variation at the nano-LiBr interface is demonstrated along the falling film's length. The interfacial heat transfer flux experiences rapid augmentation within the 0–40 mm length range of the falling film. Within the length ranges of 40–100 mm and 100–480 mm, the interfacial heat transfer flux undergoes subsequent rapid and gradual decreases. Additionally, there's an enhancement in the interfacial heat transfer flux with the introduction of nanoparticles. At a nanoparticle mass fraction of 0.15 wt%, the interface exhibits a peak heat transfer flux value of 9250 $W \cdot m^{-2}$. Initially, within the 0–40 mm length range of the falling film, the solution entering the inclined plate achieves equilibrium with water vapor. Upon entering the tube, cooling reduces the liquid film's interfacial temperature, and the absorption process releases substantial latent heat, leading to a rapid heat transfer flux increase. Subsequently, between the 40–480 mm length range of the falling film, as the cooling water temperature rises, the cooling capacity diminishes. This results in elevated solution temperature, reduced temperature gradient, and decreased heat transfer capacity.

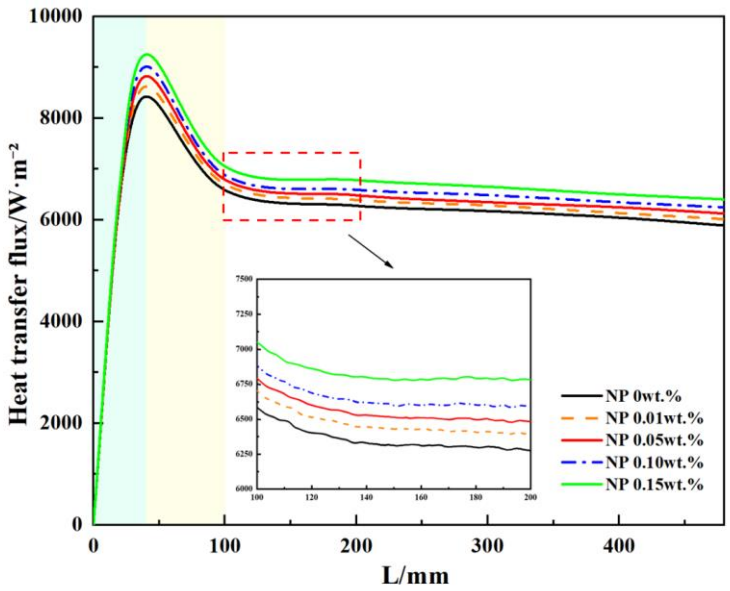

Fig. 13. Variation of interfacial heat transfer flux along the length of the falling film with nanoparticles mass fraction.

The variation of the nano-LiBr interfacial heat transfer coefficient along the falling film's length, under a flow rate of 1.0 L/min, is illustrated in Fig. 14. The interfacial heat transfer coefficient experiences rapid decline within the 0–100 mm falling film length range. Within the range of 100–480 mm, it decreases linearly. Moreover, the interfacial heat transfer coefficient shows enhancement with the addition of nanoparticles. At a nanoparticle mass fraction of 0.15 wt%, the interfacial heat transfer coefficient decreases rapidly within the range of 21.23–15.97 $W \cdot m^{-2} \cdot K^{-1}$, followed by a gradual decrease within the range of 15.97–15.01 $W \cdot m^{-2} \cdot K^{-1}$. The impact of nanoparticles on the interfacial heat transfer coefficient arises from the combined effects of particle–particle and particle–fluid interactions at the microscopic scale. The Brownian motion of the small-scale nanoparticles in the nano-LiBr leads to an increase the interfacial velocity gradient. Nanoparticle collisions further thin the boundary layer, enhancing heat transfer efficiency. Simultaneously, nanoparticles elevate the solution interface's tangential temperature gradient, altering surface tension and triggering micro-convection via the Marangoni effect, thereby intensifying the interfacial heat transfer coefficient.

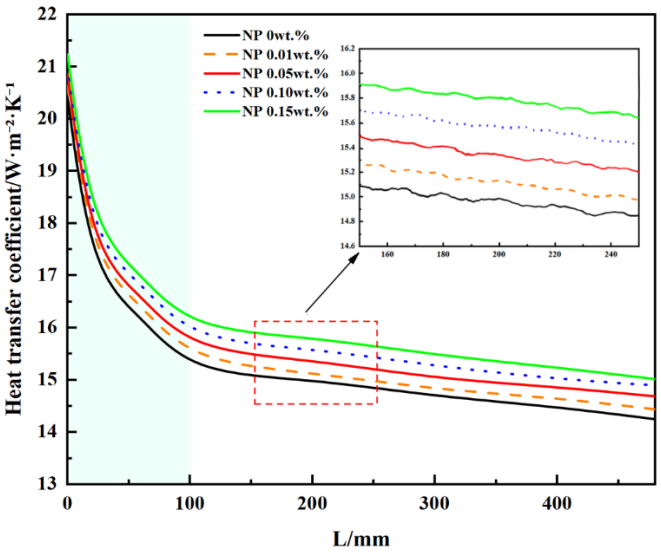

Fig. 14. Variation of interfacial heat transfer coefficient along the length of the falling film with nanoparticles mass fraction.

4.5. Mass transfer

The pattern of mass transfer flux variation at the nano-LiBr interface along the falling film's length, with a solution flow rate of 1.0 L/min, is depicted in Fig. 15. The mass transfer flux experiences a rapid increase within the 0–40 mm falling film length range. Within the ranges of 40–100 mm and 100–480 mm, the interfacial mass transfer flux drops both rapidly and gradually. The interfacial mass transfer flux exhibits an increase with the presence of nanoparticles. At a nanoparticle mass fraction of 0.15 wt%, the interface experiences a peak mass transfer flux of 0.0108 $kg \cdot m^{-2} \cdot s^{-1}$. Before entering the inclined plate, the solution and water vapor are in equilibrium. Upon contact with cooling water, the inlet solution cools, resulting in a lower saturated vapor gas pressure compared to water vapor pressure. This generates an increased gas–liquid interface driving force for mass transfer, leading to a rapid rise in the interface mass transfer flux at the entrance. However, as the absorption process progresses, solution concentration rises, mass transfer driving force decreases, and subsequently, the mass transfer flux diminishes.

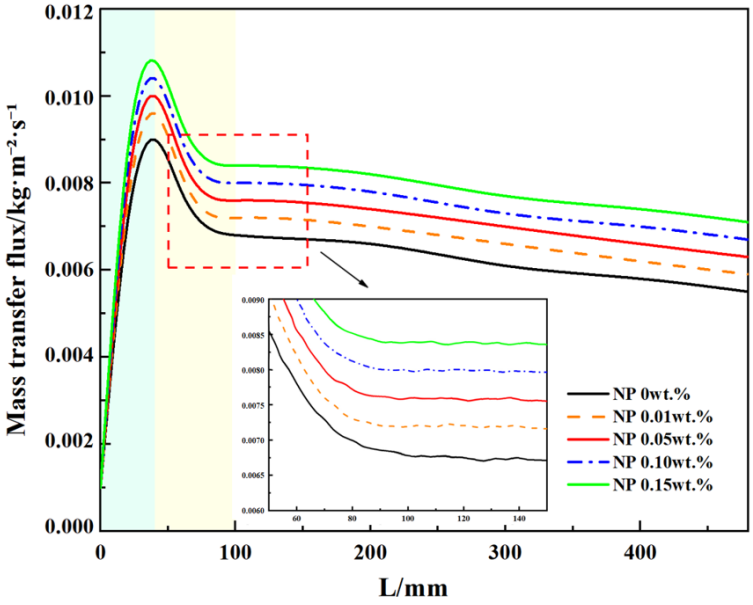

Fig. 15. Variation of interfacial mass transfer flux along the length of the falling film with nanoparticles mass fraction.

The interfacial mass transfer coefficient's variation along the falling film's length, with a solution flow rate of 1.0 L/min, is illustrated in Fig. 16. This coefficient demonstrates a decreasing trend along the inclined plate's length. Specifically, within the 0–100 mm falling film length range, the interfacial mass transfer coefficient diminishes rapidly. Subsequently, within the 100–480 mm length range, the coefficient experiences a gentler decline. Moreover, the presence of nanoparticles leads to an increase in the interfacial mass transfer coefficient.

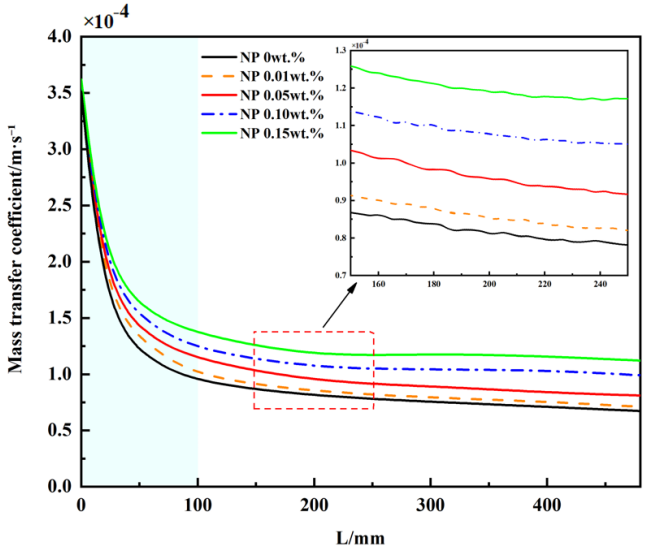

Fig. 16. Variation of interfacial mass transfer coefficient along the length of the falling film with nanoparticles mass fraction.

At a nanoparticle mass fraction of 0.15 wt%, the interfacial mass transfer coefficient experiences a rapid decrease within the range of 3.62×10^{-4}-1.35×10^{-4} $m \cdot s^{-1}$, followed by a slower decrease within the range of 1.35×10^{-4}-1.12×10^{-4} $m \cdot s^{-}1$. The main reason is primarily attributed to the nanoparticles' transport characteristics, which involve the adsorption of water vapor near the gas–liquid interface and subsequent release into the liquid phase. Furthermore, nanoparticle-induced micro-perturbations alter the interface's equilibrium state, leading to uneven concentration distribution and generating micro-convection through the Marangoni effect. As a result, the interfacial mass transfer coefficient is strengthened.

5. Conclusions

In this research, the heat and mass transfer model for falling film absorption on an inclined plate is established using the finite element method. The effect of CuO nanoparticles on the heat and mass transfer characteristics of the falling film absorption of LiBr is investigated. The key conclusions are summarized as follows.
(1) Considering the Marangoni effect, the model shows closer agreement with the experimental values, with a maximum deviation of 0.3 %. The model values are closer to the experimental values compared to the model that neglects the Marangoni effect, resulting in an approximately 29.7 % improvement in accuracy. Thus, the Marangoni effect should be incorporated when investigating the falling film absorption of nano-LiBr.

(2) The Marangoni effect is considered in the model, where the surface tension of the liquid increases the temperature gradient and concentration gradient, and therefore the heat and mass transfer fluxes are increased.
(3) The addition of nanoparticles amplifies the variations of heat and mass transfer in the inclined plate falling film absorption process. The temperature gradient with a notably greater gradient in the inlet section compared to the outlet section. The inlet section of concentration gradient showing a notably smaller gradient compared to the outlet section.

The addition of nanoparticles significantly enhances the heat and mass transfer performance of inclined falling film absorption. The peak values for interface heat transfer and mass transfer fluxes reach 9250 $W \cdot m^{-2}$ and 0.0108 $kg \cdot m^{-2} \cdot s^{-1}$.
(4) The interfacial heat transfer coefficient and mass transfer coefficient along the length of the inclined plate exhibit a two-stage reduction. Initially, the heat transfer coefficient experiences a rapid decline from 21.23 to 15.97 $W \cdot m^{-2} \cdot K^{-1}$, followed by a slower decrease from 15.97 to 15.01 $W \cdot m^{-2} \cdot K^{-1}$. Similarly, the mass transfer coefficient swiftly decreases from 3.62×10^{-4} to 1.35×10^{-4} $m \cdot s^{-1}$, followed by a gradual decrease from 1.35×10^{-4} to 1.12×10^{-4} $m \cdot s^{-1}$.

Acknowledgment

This work was supported by the National Natural Science Foundation of China [grant numbers 52006008].

References

[1] P.D. Armatis, A. Gupta, P. Sabharwall, *et al.* A chemical-absorption heat pump for utilization of nuclear power in high temperature industrial processes Int. J. Energy Res. (2021)

[2] J.H. Kai, Y.L. Peng, T.G. Walmsley, *et al.* Integration of LiBr/H_2O Absorption Heat Pump and Absorption Heat Transformer in Total Site Heat Integration Chem. Eng. Trans., 83 (2021), pp. 139-144

[3] H. Zhang, X. Liu, Y. Liu, *et al.* Energy and exergy analyses of a novel cogeneration system coupled with absorption heat pump and organic Rankine cycle based on a direct air cooling coal-fired power plant Energy, 229 (15) (2021), Article 120641

[4] S. Sehgal, J.L. Alvarado, I.G. Hassan, *et al.* A comprehensive review of recent developments in falling-film, spray, bubble and microchannel absorbers for absorption systems Renew. Sustain. Energy Rev., 142 (8) (2021), Article 110807

[5] R.B. Jaballah, M.B.B. Hamida, J. Saleh, *et al.* Enhancement of the performance of bubble absorber using hybrid nanofluid as a cooled absorption system Int. J. Numer. Meth. Heat Fluid Flow, 29 (10) (2019), pp. 3857-3871

[6] X. Wu, S. Xu, M. Jiang Development of bubble absorption refrigeration technology: A review Renew. Sustain. Energy Rev., 82 (2017), pp. 3468-3482

[7] C. Amaris, M. Valles, M. Bourouis Vapour absorption enhancement using passive techniques for absorption cooling/heating technologies: A review Appl. Energy, 231 (1) (2018), pp. 826-853

[8] X. Liang, G. He, J. Wang, *et al.* Experimental study on absorption characteristics of a falling film absorber with micro-scale NH3/LiNO3 liquid film[J] Appl. Therm. Eng., 200 (2022), Article 117719

[9] Y. Chu, M.D. Ikram, M.I. Asjad, *et al.* Influence of hybrid nanofluids and heat generation on coupled heat and mass transfer flow of a viscous fluid with novel fractional derivatives J. Therm. Anal. Calorim., 144 (2021), pp. 2057-2077

[10] S. Valiyandi, G. Thampi Review on performance analysis in diffusion absorption refrigeration system (DARS) using different working fluids[J] Int. J. Ambient Energy (2023) (just-accepted): 1–52

[11] S.Y. Jung, H. Park Experimental investigation of heat transfer of Al_2O_3 nanofluid in a microchannel heat sink Int. J. Heat Mass Transf., 179 (2021), Article 121729

[12] S.V.S. Sudheer, K.K. Kiran, K. Balasubramanian Experimental studies of heat transfer and flow regimes during flow boiling of water and alumina nanofluids at

different heat and mass fluxes Proc. Inst. Mech. Eng. C J. Mech. Eng. Sci., 233 (19–20) (2019), pp. 7155-7169

[13] T.J. Choi, S.H. Kim, S.P. Jang, *et al.* Heat transfer enhancement of a radiator with mass-producing nanofluids (EG/water-based Al2O3 nanofluids) for cooling a 100kW high power system[J] Appl. Therm. Eng., 180 (2020), Article 115780

[14] H. Kim, J. Jeong, T.K. Yong Heat and mass transfer enhancement for falling film absorption process by SiO_2 binary nanofluids Int. J. Refrig, 35 (3) (2012), pp. 645-651

[15] L. Zhang, Z. Fu, Y. Liu, *et al.* Experimental study on enhancement of falling film absorption process by adding various nanoparticles Int. Commun. Heat Mass Transfer, 92 (2018), pp. 100-106

[16] I. Shahrul, I. Mahbubul, S. Khaleduzzaman, *et al.* A comparative review on the specific heat of nanofluids for energy perspective Renew. Sustain. Energy Rev., 38 (2014), pp. 88-98

[17] G. Wang, Q. Zhang, M. Zeng, *et al.* Investigation on mass transfer characteristics of the falling film absorption of LiBr aqueous solution added with nanoparticles Int. J. Refrig, 89 (2018), pp. 149-158

[18] H.A. Mohammed, A. Al-aswadi, N. Shuaib, *et al.* Convective heat transfer and fluid flow study over a step using nanofluids: a review Renewable and Sustainable Energy Renewable and Sustainable Energy Reviews, 15 (6) (2011), pp. 2921-2939

[19] S. Krishnamurthy, P. Bhattacharya, P.E. Phelan, *et al.* Enhanced Mass Transport in Nanofluids[J] Nano Lett., 6 (3) (2006), pp. 419-423

[20] W. Wu, G. Liu, S. Chen, *et al.* Nano-ferrofluid addition enhances ammonia/water bubble absorption in an external magnetic field Energ. Buildings, 57 (2013), pp. 268-277

[21] L. Yang, K. Du, X. Niu, *et al.* Numerical investigation of ammonia falling film absorption outside vertical tube with nanofluids Int. J. Heat Mass Transf., 79 (2014), pp. 241-250

[22] A. Moghadassi, E. Ghomi, F. Parvizian A numerical study of water based Al_2O_3 and Al_2O_3-Cu hybrid nanofluid effect on forced convective heat transfer Int. J. Therm. Sci., 92 (2015), pp. 50-57

[23] L. Zhang, Y. Li, Y. Wang, *et al.* Effect of Nanoparticles on H_2O/LiBr Falling Film Absorption Process Asme International Conference on Micro/nanoscale Heat & Mass Transfer (2016), pp. 1-11

[24] M.B.B. Hamida, J. Belghaieb, N. Hajji Heat and Mass Transfer Enhancement for Falling Film Absorption Process in Vertical Plate Absorber by Adding Copper Nanoparticles Arab. J. Sci. Eng., 43 (2018), pp. 4991-5001

[25] H. Gao, F. Mao, Y. Song, *et al.* Effect of adding copper oxide nanoparticles on the mass/heat transfer in falling film absorption[J] Appl. Therm. Eng., 181 (2020), Article 115937

[26] R. Zhou, M. Wang, *et al.* Modeling and experimental verification of the enhancement of TiO2 nanofluid on ammonia falling film absorption process[J] Int. J. Therm. Sci., 184 (2023), Article 107917

[27] H. Hu Numerical Simulation and Experimental Research of Falling Film Generation with Ammonia Water Nanofluids (In Chinese) Southeast University, China, Nanjing (2015)

[28] X. Zhang, R. Manica, Q. Liu, *et al.* Inward Flow of Intervening Liquid Films Driven by the Marangoni Effect during Bubble-Solid Collisions in Ethyl Alcohol–NaCl Aqueous Solutions[J] Langmuir (2021)

[29] Y. Hu, S. Chen, J. Huang, et al. Marangoni effect on pool boiling heat transfer enhancement of self-rewetting fluid[J]. International Journal of Heat and Mass Transfer, 2018, 127 (PT. B):1263-1270.

[30] C. Li, N. Zhang, X. Wang, *et al.* Marangoni instability of an evaporating binary mixture droplet[J] Phys. Fluids, 35 (8) (2023)

[31] H. Lin Numerical simulation of the Marangoni effect (In Chinese) Xiamen University, China, Xiamen (2014)

[32] B.K. Pak, Y. Cho Hydrodynamic and heat transfer study of dispersed fluids with submicron metallic oxide particles Exp. Heat Transfer, 11 (2) (1998), pp. 151-170

[33] H.C. Brinkman The Viscosity of Concentrated Suspensions and Solutions. Chem. Phys., 20 (1952), p. 571

[34] Y. Xuan, W. Roetzel Conceptions for heat transfer correlation of nanofluids Int. J. Heat Mass Transf., 43 (19) (2000), pp. 3701-3707

[35] G. Wang, P. Dong, L. Yang, *et al.* Experimental and theoretical investigation on the surface tension of nano-Lithium Bromide solution Int. Commun. Heat Mass Transfer, 123 (2021), Article 105231

[36] A. Faghri Transport Phenomena in Multiphase Systems[M] Elsevier (2006)

[37] P. Roache Perspective: A Method for Uniform Reporting of Grid Refinement Studies J. Fluids Eng., 116 (3) (1994), pp. 405-413

[38] P.J. Boache Perspective: a method for uniform reporting of grid refinement studies J. Fluids Eng., 116 (3) (1994), pp. 405-413, 10.1115/1.2910291

[39] I. Celik, U. Ghia, P. Roache, *et al.* Procedure for estimation and reporting of uncertainty due to discretization in CFD applications J. Fluids Eng., 130 (7) (2008), Article 078001